This is an open access article published under a Creative Commons Attribution (CC-BY) License, which permits unrestricted use, distribution and reproduction in any medium, provided the author and source are cited.

Macromolecules

Article

Cite This: Macromolecules 2019, 52, 4721−4728

pubs.acs.org/Macromolecules

Water-Induced Structural Rearrangements on the Nanoscale in Ultrathin Nanocellulose Films

Calvin J. Brett,*[,†,‡,§] Nitesh Mittal,[†,‡] Wiebke Ohm,[§] Marc Gensch,[§,∥] Lucas P. Kreuzer,[∥] Volker Körstgens,[∥] Martin Månsson,[⊥] Henrich Frielinghaus,[#] Peter Müller-Buschbaum,[∥,¶] L. Daniel Söderberg,[†,‡] and Stephan V. Roth*[,§,∇]

[†]Department of Mechanics, KTH Royal Institute of Technology, Stockholm 100 44, Sweden

[‡]Wallenberg Wood Science Center, KTH Royal Institute of Technology, Stockholm 100 44, Sweden

[⊥]Department of Applied Physics, KTH Royal Institute of Technology, Stockholm 164 40, Sweden

[∇]Fibre and Polymer Technology, KTH Royal Institute of Technology, Stockholm 100 44, Sweden

[§]Deutsches Elektronen-Synchrotron DESY, Hamburg 22607, Germany

[∥]Lehrstuhl für Funktionelle Materialien, Physik-Department, and [¶]Heinz Maier-Leibnitz Zentrum (MLZ), Technische Universität München, Garching 85748, Germany

[#]Jülich Centre for Neutron Science at MLZ, Forschungszentrum Jülich GmbH, Garching 52428, Germany

Supporting Information

ABSTRACT: Many nanoscale biopolymer building blocks with defect-free molecular structure and exceptional mechanical properties have the potential to surpass the performance of existing fossil-based materials with respect to barrier properties, load-bearing substrates for advanced functionalities, as well as light-weight construction. Comprehension and control of performance variations of macroscopic biopolymer materials caused by humidity-driven structural changes at the nanoscale are imperative and challenging. A long-lasting challenge is the interaction with water molecules causing reversible changes in the intrinsic molecular structures that adversely affects the macroscale performance. Using in situ advanced X-ray and neutron scattering techniques, we reveal the structural rearrangements at the nanoscale in ultrathin nanocellulose films with humidity variations. These reversible rearrangements are then correlated with wettability that can be tuned. The results and methodology have general implications not only on the performance of cellulose-based materials but also for hierarchical materials fabricated with other organic and inorganic moisture-sensitive building blocks.

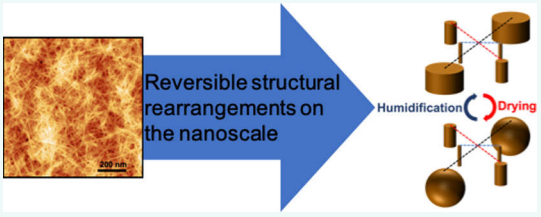

INTRODUCTION

One-dimensional (1D) nanoparticles such as nanofibers, nanowires, or nanorods attract increasing attention because of their physical properties given by their high-aspect ratio.[1] Cellulose nanofibers (CNF) are very attractive because of their earth-abundant biobased origin and biocompatibility, having favorable properties such as lightweight, thermal stability, and good mechanical strength.[2−4] These attributes make CNF a very promising precursor for the design of high-performance biobased materials and nanocomposites.[5,6] Drawbacks for biobased materials are still systematic control of quality, influence of solvent absorption, and limited life-time, compared to some fossil-based materials. However, keeping in mind the growing environmental concerns, CNFs are already finding their way to a wide range of applications from transparent conductive nanopaper to ultrastrong bio-active fibers.[7−10] Over the last decades, sustainable materials have also gained increasing attention for future flexible, biodegradable, yet disposable electronics.[11−14] Transparent cellulose nanopaper is used already in small devices because of its mechanical strength, flexibility, and conformability originated from the CNF nanosize and semiflexible nature. CNFs also yield a smoother nanopaper compared to paper made from conventional cellulose fibers.[13] In such applications, surface roughness and porosity is an important factor that affects the device compatibility, as high surface roughness may lead to inhomogeneities and a decrease in performance for thin-film-based applications as optoelectronic devices.[15−18] Industrial-style airbrush spray deposition facilitates scalable roll-to-roll compatible and transferable technology with high acceptance in the coating area, such as for sprayed flexible organic photodiodes,[19−23] being widely applied in edible coatings consisting of sprayed cellulose on fresh or processed food to prevent mold. Such coatings can also act as a partial barrier to moisture as well as to improve handling properties.[24] Tailoring of the hygroscopic behavior affects the wettability of the material, which would provide means for reducing physical degradation, for example, swelling and loss in mechanical

Received: March 15, 2019
Revised: May 17, 2019
Published: June 12, 2019

Downloaded via UNIV HAMBURG on December 13, 2019 at 01:23:45 (UTC).
See https://pubs.acs.org/sharingguidelines for options on how to legitimately share published articles.

strength. This has been shown by Li et al. who tuned wettability by incorporating polyurethane acrylate.[25]

In this work, we have investigated nanoscale morphological rearrangements in spray-deposited low-roughness hydrophilic ultrathin CNF films having switchable, tailored wettability. Atomic force microscopy (AFM) as well as optical microscopy was used to quantify the differences in the surface topography. Grazing incidence small-angle X-ray and neutron scattering (GISAXS/GISANS) are surface-sensitive scattering techniques with statistical relevance[26,27] and were employed to study the morphological features within the ultrasmooth CNF thin films under as-prepared conditions as well as their rearrangement under humidification. Contact angle measurements were conducted to resolve the surface free energy of the nanocellulose thin films fabricated with different surface charge densities of CNFs.

■ EXPERIMENTAL SECTION

Sample Preparation. CNFs were prepared from chemically bleached wood fibers (60% Norwegian spruce and 40% Scots pine, Domsjo AB, Sweden). The wood pulp fibers were chemically treated with a 2,2,6,6-tetramethylpiperidinyl-1-oxyl (TEMPO)-mediated oxidation reaction.[28] In order to obtain CNFs with different surface charge densities (400, 800, 1000, and 1360 μmol/g), we followed a protocol described elsewhere.[29] The gel-like suspensions were diluted by adding ultrapure water and mixed thoroughly using a mechanical mixer (12 000 rpm for 10 min, Ultra Turrax, IKA, Germany) and by sonication (10 min, Sonics Vibra-Cell CV33, USA). The diluted suspensions were then centrifuged (Rotina 420, Hettich GmbH & Co. KG, Germany) at 5000 rpm for 60 min. The dry content of the suspensions was determined by gravimetric analysis and adjusted to 0.07 wt %. The resulting suspension was then used for the airbrush spray deposition experiments. The average length of CNFs is around 500 nm and the diameter is around 2.5 nm.[29]

As a substrate, polished silicon (Si) wafers (Si-Mat, Germany) were used. The wafers were cut to (20 × 20) mm^2 for GISAXS measurements and (20 × 100) mm^2 for GISANS measurements. The wafers were first cleaned with solvents (ethanol, acetone, and isopropanol, all Carl Roth, Germany) and subsequently cleaned with ultrapure water (Milli-Q, 18.2 MΩ cm^{-1}), followed by an acid bath (87.5 mL hydrogen peroxide 30%, 190 mL sulfuric acid 96%, and 37.5 mL ultrapure water, all Carl Roth, Germany) at 80 °C for 15 min. This procedure yields a hydrophilic sample surface. All used chemicals are listed in the Supporting Information.

Airbrush Spray Deposition. The spray deposition experiments were performed by facilitating an airbrush spray device (Compact JAU D555000, Spray Systems, Germany) at the beamline P03 (see Figure 1). The CNF suspension was supplied by a siphon attached to the airbrush spray device.

The spray deposition was achieved through atomization of the CNF suspension with compressed nitrogen at a gas pressure of 1 bar. The nozzle-to-substrate distance of 200 mm led to spraying in the very dilute regime (see Lefebvre and McDonell[30]). We used a spray protocol as follows: 0.5 s spraying, 2 s waiting, in 20 cycles, corresponding to a film thickness $x \approx 200$ nm. Ohm et al.[31] showed that the film thickness linearly increases with the used number of spray pulses when intermittent drying is used. The Si substrate temperature was controlled to 100 °C. This protocol and the heated surface caused the films to dry evenly, suppressing visually, by the use of a microscope, any coffee-ring effects as previously shown for nanoparticles.[32−34] The GISANS samples were prepared using CNFs with 1000 μmol/g and the same above-mentioned protocol but with larger Si substrates (20 × 100) mm. To cover the full wafer, the spray nozzle was cyclic-translated 150 mm with 30 mm/s and 75 spray pulses with the above-mentioned conditions; 0.5 s spraying and 2 s waiting. This yielded the same surface roughness and thickness as the above-mentioned smaller samples proving the scalability of our approach.

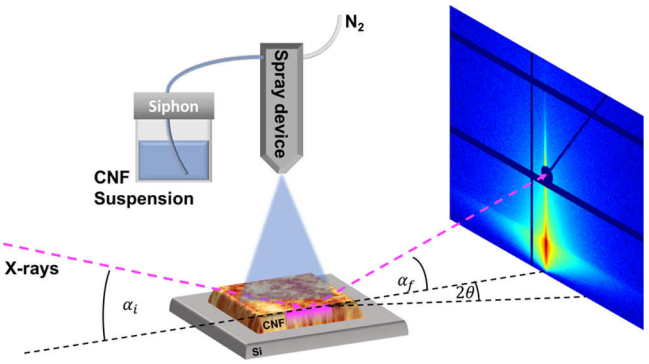

Figure 1. Schematic of the spray setup used at the synchrotron beamline P03 at DESY. In situ spray deposition is performed while analyzing the layering process with GISAXS.

Atomic Force Microscopy. The AFM measurements were conducted using a MultiMode (MMAFM-2, Bruker Corporation, USA) AFM with a silicon nitride-based cantilever for soft materials (Scanasyst-AIR-HR, resonance frequency: 130 kHz, spring constant: 0.4 N/m, Bruker Corporation, USA) with a nominal tip radius of 2 nm. The ScanAsyst mode, a tapping mode, was used to map the AFM topographical maps. The root-mean-square (rms) roughness was analyzed from the AFM topographical maps (10 × 10) μm^2. Therefore, five measurements were performed on different positions of the sample and averaged. The thin film thickness was analyzed by scratching the CNF sample surface in the middle of the wafer (see Figure S1 and Table S1).

Surface-Sensitive X-ray Scattering. The GISAXS experiments were conducted at the P03 beamline at the PETRA III synchrotron at DESY (Hamburg, Germany),[35,36] using a sample-to-detector distance, SDD = (5007 ± 1) mm with an incident photon energy of $h\nu$ = 13 keV (λ = 0.9537 Å) and a beam size of ($H \times V$, 16 × 22) μm^2. In order to observe the complete scattering pattern, a 2D pixel detector PILATUS 1M (Dectris Ltd., Switzerland) was used, with a pixel size of (172 × 172) μm^2 and (981 × 1043) pixels^2 for the GISAXS measurements. The high-resolution GISAXS measurements were conducted at the same geometry with a 2D pixel detector LAMBDA 750K (X-spectrum, Germany) with a pixel size of (55 × 55) μm^2 and (512 × 1536) pixels^2. The X-ray angle of incidence was set to α_i = (0.41 ± 0.01)° in order to penetrate the whole film thickness. Each GISAXS pattern was exposed for 0.5 s and a lateral scanning step size of 100 μm was used for avoiding radiation damage (see Figures S2 and S3). 1D intensity distributions were extracted from the 2D GISAXS pattern (see Figure S4) using the DPDAK software package and later fitted using minimum chi-square estimation with a cylindrical form factor as previously introduced by Schaffer et al.[37−39]

Surface-Sensitive Neutron Scattering. The GISANS experiments were conducted at the KWS-1 instrument operated by the Jülich Centre for Neutron Science (JCNS) at the research reactor FRM II at the Heinz Maier-Leibnitz Zentrum (Garching, Germany).[40,41] A SDD = 3.7 m was used with an incident neutron wavelength of λ = 5 Å using a 10% wavelength selector and a beam size of (10 × 1) mm^2. The detector was a two-dimensional Li-scintillation anger camera with a pixel size of (5 × 5) mm^2 and (112 × 112) pixels^2. The neutron incidence angle was set to α_i = (1 ± 0.01)°. Acquisition time for each GISANS pattern was 2 h. Analogous data treatment procedures were done as explained in the GISAXS part. For the GISANS experiments, a humidity-controlled (0−90% RH) sample chamber was used. Changes between humidity to equilibrium take up to 20 min; another hour was waited prior to the individual measurements to ensure full hydration or drying.

Contact Angle Measurements. Sessile-drop contact angle measurements were made to monitor the wettability on the different charged cellulose thin films, using an OCA20 (Data Physics, Germany) contact angle measurement system. The volume of the drops was controlled with an automatic syringe system to 1 μL. To

DOI: 10.1021/acs.macromol.9b00531
Macromolecules 2019, 52, 4721−4728

calculate the free surface energy within the Owens, Wendt, Rabel and Kaelble (OWKR)[42] method, three different polar and unpolar solvents were used, starting with ultrapure water (Milli-Q, 18.2 MΩ cm^{-1}), ethylene glycol (>98%, Carl Roth, Germany), and diiodomethane (≥99.4%, VWR, USA). The polar and dispersive components can be found in Table S2. Five droplets for each solvent were placed and the contact angles on both sides from each measurements were averaged for the surface free energy calculations later on. The contact angles are shown exemplary for the four different charge densities in Figure S5. All calculations were done within the software SCA20 (Data Physics, Germany).

■ RESULTS AND DISCUSSION

Topographical Information. The AFM images show a smooth, closely packed thin film (Figure 2a−d). Dai et al.

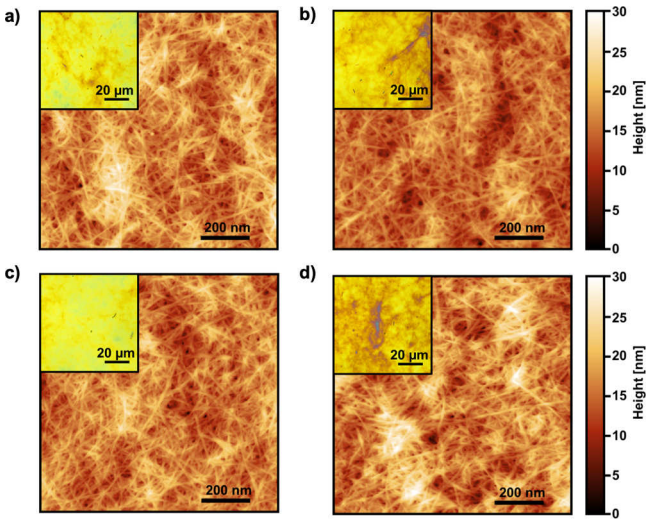

Figure 2. AFM topographic images with four different surface charges: (a) 400, (b) 800, (c) 1000, and (d) 1360 μmol/g. The insets are optical microscopy images of the corresponding films.

successfully showed the use of cellulose nanopaper as a dielectric material for low-voltage field-effect transistors. The transistor is fully functional even under bending, which underlines the good-networking properties while staying flexible.[9] Thin film flexibility and toughness can only be achieved if the film forms a densely packed network with little defects. The advantage when using spray deposition is that we could tailor the thickness while retaining the densely packed CNF network. No observable differences in the appearance of film morphology due to the influence of the different surface charges are noticed from the AFM mapping. For all cases, the nanofibers are well distributed into a web structure without obvious agglomeration or large-scale domains. By resolving individual fibers, one can study the alignment over the sample area and we cannot observe any preferential alignment from the center to the outer regions of the thin film caused by the spray conditions. The thin CNF film is very homogeneous in fibril distribution without variation toward the outer regions of the spray cone. The film thickness of all samples is constant (191 ± 5 nm) (Table S1). However, the optical microscopy images for all four cases in Figure 2 show larger entities as brighter spots, which stem from bigger agglomerates of CNFs.

The radial power spectral density (PSD) is fitted using a cylindrical form factor approximation with paracrystalline order (see Figure S6 and Table S3), which visualizes the morphological changes on the surface due to the radially disordered morphology on the surface topography (see Figure S7).[38] In the region below 0.008 nm^{-1}, slight differences between the films can be observed, which may be attributed to the structures at the resolution of PSD distribution. Within the resolved scales, one finds medium-sized structures on the surface with a radius of r_{AFM} = (26.7 ± 0.5) nm in a distance of d_{AFM} = (69 ± 16) nm to each other, which do not change with surface charge.

Figure 3 presents the rms roughness of the fabricated thin films plotted for the four different surface charges and

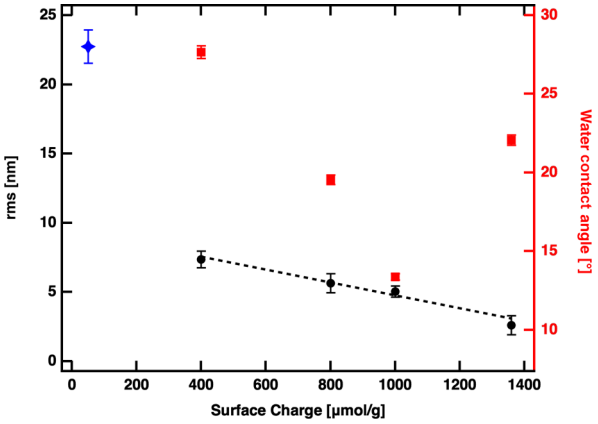

Figure 3. rms in nanometer of the roughness (black, blue) and the water contact angle (red) of the different charged cellulose thin films. The trend of the roughness is linearly fitted for better visualization (dashed line). The blue diamond is a comparison to spray deposited enzymatic CNFs with similar thickness.[31]

compared to our previous results for sprayed enzymatic cellulose thin films.[31] The graph shows that the surface roughness of the thin films decreases following a linear decay with increasing surface charge of the CNFs, see eq 1 in Supporting Information. The graph includes also the contact angle of water as a function of surface charge. The contact angle decreases linearly from ≈27° to ≈14° when changing surface from 400 to 1000 μmol/g respectively. This feature can be attributed to the decreased surface roughness. When the roughness decreases even more, the contact angle, however, raises up to ≈22°, which we speculate is driven by the increased ionic strength. Ahola et al. and Qi et al.[43,44] showed that for spin-coated layer-by-layer fabricated thin films, the roughness depends on the charge, from 4 nm for low surface charge to 2−3 nm with high surface charge. They also found that low-charged CNFs do not form a densely packed thin film but rather a loose network. Sprayed CNFs made of enzymatic cellulose show a surface roughness of around (23 ± 1) nm when prepared under similar conditions, having a surface charge of around 50 μmol/g.[45] This corresponds to the difficulties in the fibrillation process of enzymatic CNF, which typically results in agglomerates, compared to the well-dispersed fibers in the case of highly charged TEMPO−CNF. In the present experiments, the lowest roughness of (2.5 ± 0.6) nm was found for the highest surface charge (1360 μmol/g) on a large-scale of 20 × 100 mm. Here, we assumed the highest roughness due to repulsion of the single fibers from each other, which clearly does not seem to be the case. This may instead be attributed to an ordering effect via repulsion. Benselfelt et al. found in a drop-casted self-assembly study of CNFs on a substrate no obvious correlation between

DOI: 10.1021/acs.macromol.9b00531
Macromolecules 2019, 52, 4721−4728

roughness and higher surface charges.[46] Félix et al. confirmed stratification in spray-deposited multilayer thin films using neutron reflectometry.[47] They tuned the distance between layers and could thereby prove a super-lattice structure. We assume that the additional surface charge of the CNF used in our investigations allows for an improved smoothening. We deduce that the layering process is improved when intermittent drying in between single spray pulses occurs as earlier described for enzymatic CNF by Ohm et al.[31] and for polystyrene colloids by Zhang et al.[32] The increased surface temperature during spray deposition results in a fast solvent evaporation, which inhibits the aggregation of nanocolloids and yields smooth monolayers, as shown previously by Zhang et al.[32] During spraying, we deposit small droplets of CNF suspension on the heated substrate, and the droplets coalesce and dry. The resulting thin film thus consists of many coalesced droplets, and because of increased temperature, the small droplets do not form any type of visual coffee-ring effect. Apparently, the highest surface charge promotes nanofiber assembly in such a way that nanoscale building blocks form a uniform and homogeneous densely packed film with unprecedented low roughness compared to typical spray-deposited thin films. This demonstrates that the surface roughness of spray-deposited thin films can be tuned by varying surface charge density of the building blocks.[19] Nordenström et al. argued that increasing surface charge density of the CNF suspensions promotes an electrostatic stabilization of the system, which is beneficial for the non-agglomerating self-assembly of the films.[48] Water evaporation caused a rapid concentration increase of the CNF suspension causing increased ionic strength leading to gel formation, followed by an immediate lock-in, which we hypothesize is the driving force for the smoothing of our spray-deposited thin films.

Thin Film Morphology. In order to investigate the inner morphology of the spray-deposited CNF thin films, GISAXS measurements were performed on all samples, providing a possibility to probe all relevant length scales from nano- to microscale, which is beneficial for characterizing the layering process.[27] Because of the penetration depth of GISAXS, one obtains information on both the surface morphology and the self-assembly within the thin film. Figure S8a−d depicts the 2D GISAXS pattern of the four different CNF films. The inset shows a high-resolution zoom-in of the region around the critical angle of the materials (Yoneda region,[49] see Supporting Information for details). The angle of incidence $\alpha_{in} = (0.41 \pm 0.01)°$ is well above the critical angle $\alpha_{crit,CNF} = (0.13 \pm 0.01)°$, and accordingly the whole film thickness is probed. The value found for the critical angle is in good agreement with the theoretical value for cellulose of $\alpha_{crit,cellulose} = 0.12°$,[31] and the deviation of $\alpha_{crit,\Delta} = 0.01°$ can be attributed to the nanosized structured fibers in comparison to bulk cellulose.

Two distinct line cuts (see Supporting Information) were performed on the GISAXS pattern, a horizontal integration in q_z-direction and a vertical integration in q_y-direction, respectively, shown in Figure 4a,b (details see Figure S4). From these two line cuts, one is able to deduce the thin film morphology parallel and vertical to the surface. The 1D intensity distribution along q_y is fitted with a model using upright standing cylinders with a radius r_i and a distance from center-to-center of d_i similar to the PSD fitting. This is the best approximation of scattering centers for the scattered intensity, for details see the inset of Figure 4a. The index $i = 1, 2$ shows

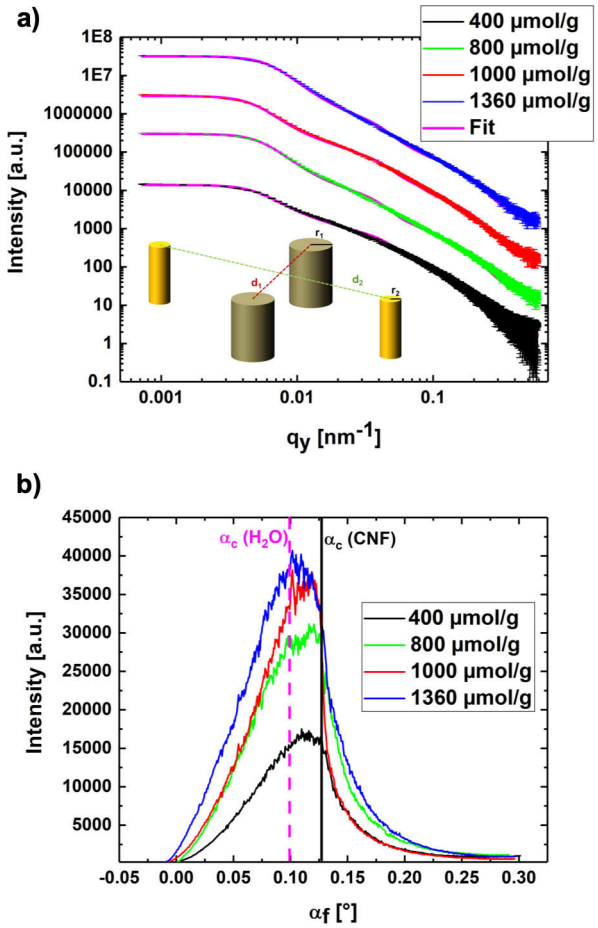

Figure 4. (a) Intensity distribution along q_y at the Yoneda region of cellulose $\alpha_{crit,CNF} = 0.13°$ for four different surface charges (black 400 μmol/g, green 800 μmol/g, red 1000 μmol/g, and blue 1360 μmol/g). The inset shows the used cylindrical model represented by two different sized cylinders with different distances from each other. For better visualization, the graphs are vertically shifted. (b) Intensity distribution as a function of q_z along $q_y = 0$ nm^{-1}. The dashed magenta line shows the Yoneda region of $\alpha_{crit,H_2O} = 0.094°$, and the black line shows the critical angle of cellulose.

the values for two-domain feature sizes, which we found in the film morphology. This model represents a projection of the internal structure of the film onto the surface, that is, it is directly coupled to the two-dimensional representation of the models used for evaluating the scattering results. This approximation provides a tool to be used on complementary methods as AFM, GISAXS, and GISANS. The fit results are shown in Table S4. Two characteristic structural entities can be found in the film, which we attribute to the agglomeration of CNFs, the larger with $r_1 \approx 27$ nm in a distance of $d_1 \approx 60$ nm and the smaller entities of $r_2 \approx 7.5$ nm in a distance of $d_2 \approx 70$ nm. It should be noted that due to the process of centrifugation during the preparation of CNFs, one filters out larger untreated pulp fibers, so the resulting agglomerates are formed in the film during drying and are not present in the initial dispersion.

In the q_z-direction, the critical angle is extracted from the decrease above $\alpha_{crit,CNF} = (0.13 \pm 0.01)°$. The presence of the substrate in our films is negligible, as the intensity observed in Yoneda-region (scattering maximum in the diffuse scattering when the scattering angle is approximately the critical angle)

DOI: 10.1021/acs.macromol.9b00531
Macromolecules 2019, 52, 4721−4728

for silicon $\alpha_{crit,Si}$ = 0.137° and silica α_{crit,SiO_2} = 0.133° is low compared to the scattering of the CNF film. Around α_f = (0.10 ± 0.01)°, we observe a narrow intensity increase, which can be attributed to a material using the complex X-ray refractive index $n = 1 - \delta + i\beta$. We thus deduce a dispersion of $\delta = 1.49 \times 10^{-6}$, which is in good agreement with water $\delta_{H_2O} = 1.36 \times 10^{-6}$ at a density of 1 g/cm^3 corresponding to a critical angle of α_{crit,H_2O} = 0.094°. Attributing this critical angle to water, it is qualitatively argued that the water content is increasing with surface charge density and is not fully evaporating as assumed due to the high temperature of 100 °C applied to the substrate during spray deposition. Sjöstedt et al. could see the same trend in water retention value measurements of TEMPO–CNF suspensions with increasing surface charge.[50]

Furthermore, GISANS experiments were performed to elucidate in situ water uptake and release as well as to prove the large scale homogeneity in the as-prepared CNF thin films. In this context, in situ refers to the fact that the experiments are performed during humidification. AFM measurements confirm that the roughness of rms = 4.9 ± 0.5 nm is not changed using CNFs with 1000 μmol/g for the upscaling to (20 × 100) mm^2 wafers. During the GISANS measurements, the CNF thin film with a surface charge of 1000 μmol/g is dried in a humidity-controlled measurement chamber to relative humidity (RH) 0%, humidified with D_2O to 90% and redried to 0%. At 90 and 0% RH, a GISANS measurement is performed (see Figures 5a, S9 and S10, Table S5). The 1D intensity distribution is then fitted with the same model used for the PSD similarly to the GISAXS measurements (see Figure 5b). The resulting parameters at the dry state before and after humidification are overlapping within the error bars

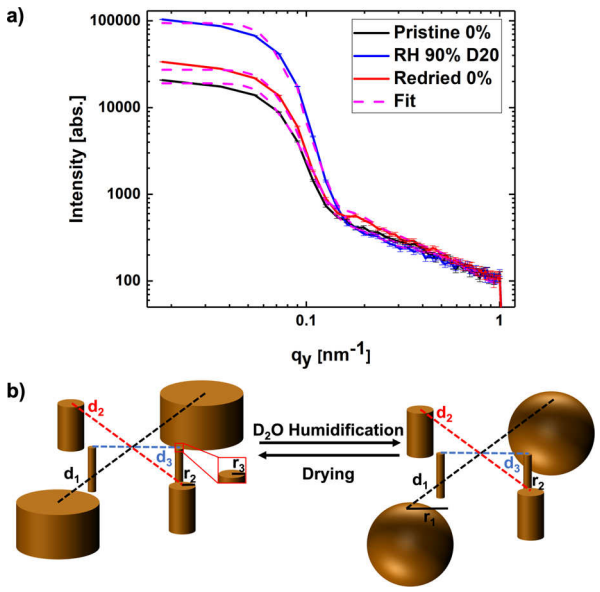

Figure 5. (a) Horizontal line cuts of the 2D GISANS data taken at the critical angle for CNF with 1000 μmol/g at α_i = 1° in (a) for the dry, the hydrated (RH 90%), and the redried sample. The pristine and the redried samples are fitted using the cylindrical model approximation on a paracrystal (dashed lines). The intensity difference and the increased intensity at ≈0.2 nm^{-1} in pristine and redried films can be attributed to residual D_2O molecules in the CNF thin film. Because of hydration, only the largest entities are changing from a cylinder to a spherical structure, which is schematically illustrated in (b).

with the previous measurements, see Table S5. Additionally, because of the larger accessible q-range of the GISANS experiment, a scattering signal from single CNFs could be resolved giving one more characteristic scale with a radius of r_3 ≈ 2.5 nm in a distance of d_3 ≈ 8 nm, which we attribute to the dimensions of the individual CNFs;[29] for more details, see Table S5. Additionally, during humidification, we observe that the largest agglomerates of CNFs now appear as spherical objects in the scattering pattern with no change in the radius, but with an increase in distance to each other, see Figure S11 and Table S5. The physical interpretation of the change from a cylindrical to a spherical shape corresponds to the change in the structure from two-dimensional to three-dimensional shape. In the present study, only the projection in lateral dimensions is fitted. It should also be noted that the humidification with D_2O increased also the contrast within the film. Previous GISAXS measurements by Ehmann et al., who studied the supramolecular rearrangement of trimethylsilyl cellulose under HCl influence, found that pores inside the film either increase in size or increase their distance, as seen in a densification process.[51] We can confirm that the largest pores or agglomerates increase their separation distance while smaller domains remain constant during humidification. We believe that the large pores or voids are either getting filled during humidification with D_2O vapor or D_2O condenses at their inner surface; both effects increase the contrast, as well as a slight expansion. The smaller features which we observe are suggested to be agglomerates of CNFs, which do not vary during humidification. Previous studies have revealed that on the nanoscale, amorphous regions of cellulose[52,53] are more sensitive to water because of higher accessibility of hydroxyl groups per unit area compared to semicrystalline CNFs[54] or crystalline cellulose nanocrystals.[55] However, on the micrometer scale, the accessibility of hydroxyl groups to water also depends on the packing of nanocellulose building blocks, which is highly dependent on the processing technique. Langmuir–Schaefer deposition is most favorable in order to induce a high packing density, however at low deposition speed, whereas spin-coating is faster, where the rapid drying kinetics and high shear flows hinder self-assembly of nanocellulose into densely packed structures.[52] Spray deposition on the other hand, is a highly versatile technique, where packing density and alignment can be tuned by controlling the processing parameters adapting to the requirements for a wide range of applications.[19,56]

Wettability. We expect an influence of the surface charge and roughness on the wetting behavior of the CNF thin film. According to Young's equation,[57] there is a relation between the surface tension of a liquid σ_{lg}, the interfacial tension σ_{sl} between a solid (s) and a liquid (l), the contact angle Θ, and the surface free energy σ_{sg} between a solid and a gas (g)

$$\sigma_{sg} = \sigma_{sl} + \sigma_{lg} \cdot \cos \Theta \tag{1}$$

According to OWKR,[42] one can use the geometrical average of the dispersive (δ) and polar (p) components of the surface tensions as

$$\sigma_{sl} = \sigma_s + \sigma_l - 2\sqrt{\sigma_s^{\delta}\sigma_l^{\delta}} - 2\sqrt{\sigma_s^{p}\sigma_l^{p}} \tag{2}$$

Combining eqs 1 and 2 yields a linear equation. Using the polar and dispersive components of the used test liquids, one can calculate the surface free energy.[42] The polar interaction describes the Coulomb interaction between permanent or

DOI: 10.1021/acs.macromol.9b00531
Macromolecules 2019, 52, 4721−4728

induced dipoles as hydrogen bonds, while the dispersive interaction stems from van der Waals interactions.[58] We find a nearly constant, slightly decreasing behavior when increasing the surface charge density of the CNF thin film for the dispersive free surface energy (see Figure 6) (red linear fit).

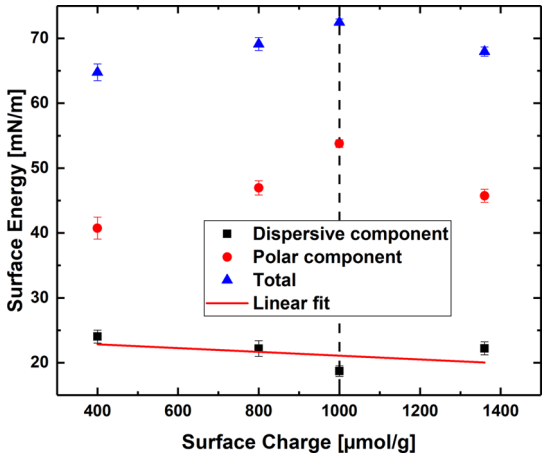

Figure 6. Free surface energy calculated by the OWRK-method[42] from the contact angle on the four different cellulose thin films. The data are shown in the individual dispersive (black) and the polar (red) component as well as the total surface free energy (blue). Linear fit of the dispersive component (red line) shows a small minimum at 1000 μmol/g, marked with the vertical black dashed line.

Clear changes in the polar component (red circles) of the surface free energy with a maximum at 1000 μmol/g are observed. We conclude that up to a surface charge of 1000 μmol/g the roughness plays the major role in the surface free energy as both the contact angle and roughness decrease simultaneously. At lower roughnesses and increasing surface charge density, surface repulsion is dominant in the system (see Figure 3). The total surface free energy is only slightly changed but follows the trend of the polar component. Tailoring the wettability could be crucial for functionalization of these thin films, for example as storage for polar solvents as those are drawing increasing attention in organic photovoltaics (OPVs) as green alternative light harvesting materials[59] or in batteries.[60]

Conventional cellulose fibers as used in paper fulfill all requirements to enable low-cost OPVs, as it is lightweight, biodegradable, and inexpensive because of its earth abundant nature. Paper's biggest advantage is that it is already widely used in large-scale industrial processes, for example, in printing.[12] We show with spray deposition a fully scalable technique combining all the advantages CNFs nature gives us. Especially for the emerging flexible electronics applications, physical properties such as low roughness, mechanical strength, porous structure, and attraction to liquids are a challenge. Our work shows an approach to further understand and enhance properties such as roughness and contact angle. Kontturi et al.[52] have previously shown that surface roughness of ultrathin amorphous cellulose films had no influence on the contact angle. Elaborating further on the impact of surface charge on the contact angle, the Wenzel equation was used to calculate the Young's contact angle, which is roughness-independent (see Figure S12).[61] An almost linear decrease in the Young's contact angle is observed, clearly implicating that the contact angle is now only dependent on surface charge density. For example, on OPV templates one also need to consider that it needs to provide mechanical strength and does not need to have any intrinsic electronic function. The porous structure of the CNF thin film was elucidated by quantifying the nature of the voids; in addition, the change in contact angle as a function of the CNF surface charge, resulting in stratified films of tailored roughness, was quantified. The contact angle influences the inhibition behavior of solvents used for depositing or printing functional layers on CNF thin film or nanopapers; the knowledge of both features is thus potentially important for tailoring transparency in OPV applications.

■ CONCLUSIONS

We demonstrate a facile route to prepare large-scale cellulose-based nanostructured thin films with a low surface roughness down to 2.5 nm on (20 × 100) mm^2 substrates. This is obtained through the surface topography of a densely packed CNF network. No differences were observed in the layering of the individual CNFs while changing the surface charge densities. It can be concluded that increasing ionic strength is highly beneficial for the layering mechanism as it directly influences the self-assembly process, which results in a low roughness. Furthermore, we observed distinct domains of smaller cellulose bundles and larger bundles or agglomerates within the thin film. By studying in situ the humidification and drying of CNFs, we observed that domains reversibly change from cylindrical to spherical appearance. With decreasing values of surface roughness corresponding to increasing surface charge densities of CNF films, the surface free energy is observed to be tunable. These features and knowledge can be used to promote the use of polar solvents in applications such as organic solar cells and to further enhance physical properties and materials lifetime.

■ ASSOCIATED CONTENT

Supporting Information

The Supporting Information is available free of charge on the ACS Publications website at DOI: 10.1021/acs.macromol.9b00531.

Analysis of atomic force microscopy data including rms roughness evaluation; AFM height profile; GISAXS beam damage evaluation; GISAXS translation scan; GISAXS integration region on the lambda detector for CNF; contact angle measurements; PSD fitting with cylindrical form factor approximation; PSD from AFM; GISAXS scattering patterns; GISANS integration region for dry CNF; vertical line cut of the GISANS data; spherical versus cylindrical approximation fit; CNF thickness; polar and dispersive components of test liquids; AFM fitting results; GISAXS fitting results for four different surface charges; GISANS fitting results; and used chemicals for the TEMPO process and substrate cleaning (PDF)

■ AUTHOR INFORMATION

Corresponding Authors

*E-mail: calvinbr@kth.se (C.J.B.).
*E-mail: svroth@kth.se (S.V.R.).

ORCID

Calvin J. Brett: 0000-0001-5789-6299
Marc Gensch: 0000-0001-5514-8158

DOI: 10.1021/acs.macromol.9b00531
Macromolecules 2019, 52, 4721−4728

Lucas P. Kreuzer: 0000-0002-9669-2130
Volker Körstgens: 0000-0001-7178-5130
Henrich Frielinghaus: 0000-0002-8812-8783
Peter Müller-Buschbaum: 0000-0002-9566-6088
L. Daniel Söderberg: 0000-0003-3737-0091
Stephan V. Roth: 0000-0002-6940-6012

Notes

The authors declare no competing financial interest.

■ ACKNOWLEDGMENTS

We thank Jan Rubeck for support during the synchrotron measurements. The authors thank the synchrotron light source PETRA III and the beamline P03 at Deutsches Elektronen-Synchrotron (DESY) for beam time allocation. C.J.B. and S.V.R. acknowledge the kind financial support from the DESY strategic fund (DSF) "Investigation of processes for spraying and spray-coating of hybrid cellulose-based nanostructures". DESY is a member of the Helmholtz Association (HGF). The research has been funded by the Knut and Alice Wallenberg Foundation through Wallenberg Wood Science Center at KTH. V.K. and P.M.-B. thank the Excellence Cluster Nanosystems Initiative Munich (NIM) and the Center for NanoScience (CeNS). L.P.K. acknowledges funding by the BMBF project 05K16WOA—FlexiProb. M.M. was partly supported by Marie Skłodowska-Curie Action, International Career Grant through the European Commission and Swedish Research Council (VR), grant no. INCA-2014-6426 as well as a VR neutron project grant (BIFROST, Dnr. 2016-06955) and the Carl Tryggers Foundation for Scientific Research (CTS-16:324).

■ REFERENCES

(1) Hu, H.; Pauly, M.; Felix, O.; Decher, G. Spray-assisted Alignment of Layer-by-Layer Assembled Silver Nanowires: A General Approach for the Preparation of Highly Anisotropic Nano-composite Films. *Nanoscale* **2017**, *9*, 1307−1314.

(2) Benítez, A. J.; Walther, A. Cellulose Nanofibril Nanopapers and Bioinspired Nanocomposites: A Review to Understand the Mechanical Property Space. *J. Mater. Chem. A* **2017**, *5*, 16003−16024.

(3) Merindol, R.; Diabang, S.; Felix, O.; Roland, T.; Gauthier, C.; Decher, G. Bio-inspired Multiproperty Materials: Strong, Self-healing, and Transparent Artificial Wood Nanostructures. *ACS Nano* **2015**, *9*, 1127−1136.

(4) Keckes, J.; Burgert, I.; Frühmann, K.; Müller, M.; Kölln, K.; Hamilton, M.; Burghammer, M.; Roth, S. V.; Stanzl-Tschegg, S.; Fratzl, P. Cell-wall Recovery After Irreversible Deformation of Wood. *Nat. Mater.* **2003**, *2*, 810−813.

(5) Wang, Q.; Du, H.; Zhang, F.; Zhang, Y.; Wu, M.; Yu, G.; Liu, C.; Li, B.; Peng, H. Flexible Cellulose Nanopaper with High Wet Tensile Strength, High Toughness and Tunable Ultraviolet Blocking Ability Fabricated from Tobacco Stalk via a Sustainable Method. *J. Mater. Chem. A* **2018**, *6*, 13021−13030.

(6) Mittal, N.; Ansari, F.; Gowda.V, K.K.; Brouzet, C.; Chen, P.; Larsson, P. T.; Roth, S. V.; Lundell, F.; Wågberg, L.; Kotov, N. A.; Söderberg, L. D. Multiscale Control of Nanocellulose Assembly: Transferring Remarkable Nanoscale Fibril Mechanics to Macroscale Fibers. *ACS Nano* **2018**, *12*, 6378−6388.

(7) Hamedi, M. M.; Hajian, A.; Fall, A. B.; Håkansson, K.; Salajkova, M.; Lundell, F.; Wågberg, L.; Berglund, L. A. Highly Conducting, Strong Nanocomposites Based on Nanocellulose-Assisted Aqueous Dispersions of Single-Wall Carbon Nanotubes. *ACS Nano* **2014**, *8*, 2467−2476.

(8) Mittal, N.; Jansson, R.; Widhe, M.; Benselfelt, T.; Håkansson, K. M. O.; Lundell, F.; Hedhammar, M.; Söderberg, L. D. Ultrastrong and Bioactive Nanostructured Bio-Based Composites. *ACS Nano* **2017**, *11*, 5148−5159.

(9) Dai, S.; Chu, Y.; Liu, D.; Cao, F.; Wu, X.; Zhou, J.; Zhou, B.; Chen, Y.; Huang, J. Intrinsically Ionic Conductive Cellulose Nanopapers Applied as All Solid Dielectrics for Low Voltage Organic Transistors. *Nat. Commun.* **2018**, *9*, 2737.

(10) Jämsä, M.; Kosourov, S.; Rissanen, V.; Hakalahti, M.; Pere, J.; Ketoja, J. A.; Tammelin, T.; Allahverdiyeva, Y. Versatile Templates from Cellulose Nanofibrils for Photosynthetic Microbial Biofuel Production. *J. Mater. Chem. A* **2018**, *6*, 5825−5835.

(11) Jung, Y. H.; et al. High-performance Green Flexible Electronics Based on Biodegradable Cellulose Nanofibril Paper. *Nat. Commun.* **2015**, *6*, 7170.

(12) Leonat, L.; White, M. S.; Głowacki, E. D.; Scharber, M. C.; Zillger, T.; Rühling, J.; Hübler, A.; Sariciftci, N. S. 4% Efficient Polymer Solar Cells on Paper Substrates. *J. Phys. Chem. C* **2014**, *118*, 16813−16817.

(13) Du, X.; Zhang, Z.; Liu, W.; Deng, Y. Nanocellulose-based Conductive Materials and their Emerging Applications in Energy Devices - A Review. *Nano Energy* **2017**, *35*, 299−320.

(14) Zhao, D.; Zhang, Q.; Chen, W.; Yi, X.; Liu, S.; Wang, Q.; Liu, Y.; Li, J.; Li, X.; Yu, H. Highly Flexible and Conductive Cellulose-Mediated PEDOT:PSS/MWCNT Composite Films for Supercapacitor Electrodes. *ACS Appl. Mater. Interfaces* **2017**, *9*, 13213−13222.

(15) Berman, D.; Guha, S.; Lee, B.; Elam, J. W.; Darling, S. B.; Shevchenko, E. V. Sequential Infiltration Synthesis for the Design of Low Refractive Index Surface Coatings with Controllable Thickness. *ACS Nano* **2017**, *11*, 2521−2530.

(16) Chen, S.; Kwok, H. S. Light Extraction from Organic Light-emitting Diodes for Lighting Applications by Sand-blasting Substrates. *Opt. Express* **2010**, *18*, 37.

(17) Gaynor, W.; Burkhard, G. F.; McGehee, M. D.; Peumans, P. Smooth Nanowire/Polymer Composite Transparent Electrodes. *Adv. Mater.* **2011**, *23*, 2905−2910.

(18) Jonda, C.; Mayer, A. B. R.; Stolz, U.; Elschner, A.; Karbach, A. Surface Roughness Effects and their Influence on the Degradation of Organic Light Emitting Devices. *J. Mater. Sci.* **2000**, *35*, 5645−5651.

(19) Richardson, J. J.; Bjornmalm, M.; Caruso, F. Technology-driven Layer-by-Layer Assembly of Nanofilms. *Science* **2015**, *348*, 2491.

(20) Falco, A.; Cinà, L.; Scarpa, G.; Lugli, P.; Abdellah, A. Fully-sprayed and Flexible Organic Photodiodes with Transparent Carbon Nanotube Electrodes. *ACS Appl. Mater. Interfaces* **2014**, *6*, 10593−10601.

(21) Krantz, J.; Stubhan, T.; Richter, M.; Spallek, S.; Litzov, I.; Matt, G. J.; Spiecker, E.; Brabec, C. J. Spray-Coated Silver Nanowires as Top Electrode Layer in Semitransparent P3HT:PCBM-Based Organic Solar Cell Devices. *Adv. Funct. Mater.* **2013**, *23*, 1711−1717.

(22) Vak, D.; Kim, S.-S.; Jo, J.; Oh, S.-H.; Na, S.-I.; Kim, J.; Kim, D.-Y. Fabrication of Organic Bulk Heterojunction Solar Cells by a Spray Deposition Method for Low-cost Power Generation. *Appl. Phys. Lett.* **2007**, *91*, 081102.

(23) Abdellah, A.; Fabel, B.; Lugli, P.; Scarpa, G. Spray Deposition of Organic Semiconducting Thin-films: Towards the Fabrication of Arbitrary Shaped Organic Electronic Devices. *Org. Electron.* **2010**, *11*, 1031−1038.

(24) Andrade, R. D.; Skurtys, O.; Osorio, F. A. Atomizing Spray Systems for Application of Edible Coatings. *Compr. Rev. Food Sci. Food Saf.* **2012**, *11*, 323−337.

(25) Li, W.; Wu, Y.; Liang, W.; Li, B.; Liu, S. Reduction of the Water Wettability of Cellulose Film Through Controlled Heterogeneous Modification. *ACS Appl. Mater. Interfaces* **2014**, *6*, 5726−5734.

(26) Müller-Buschbaum, P. GISAXS and GISANS as Metrology Technique for Understanding the 3D Morphology of Block Copolymer Thin Films. *Eur. Polym. J.* **2016**, *81*, 470−493.

(27) Roth, S. V. A Deep Look Into the Spray Coating Process in Real-time and the Crucial Role of X-rays. *J. Phys.: Condens. Matter* **2016**, *28*, 403003.

DOI: 10.1021/acs.macromol.9b00531
Macromolecules 2019, 52, 4721−4728

(28) Isogai, A.; Saito, T.; Fukuzumi, H. TEMPO-oxidized Cellulose Nanofibers. *Nanoscale* **2011**, *3*, 71−85.
(29) Geng, L.; Mittal, N.; Zhan, C.; Ansari, F.; Sharma, P. R.; Peng, X.; Hsiao, B. S.; Söderberg, L. D. Understanding the Mechanistic Behavior of Highly Charged Cellulose Nanofibers in Aqueous Systems. *Macromolecules* **2018**, *51*, 1498−1506.
(30) Lefebvre, A. H.; McDonell, V. G. *Atomization and Sprays*; CRC press, 2017.
(31) Ohm, W.; Rothkirch, A.; Pandit, P.; Körstgens, V.; Müller-Buschbaum, P.; Rojas, R.; Yu, S.; Brett, C. J.; Söderberg, D. L.; Roth, S. V. Morphological Properties of Airbrush Spray-deposited Enzymatic Cellulose Thin Films. *J. Coat. Technol. Res.* **2018**, *15*, 759.
(32) Zhang, P.; Santoro, G.; Yu, S.; Vayalil, S. K.; Bommel, S.; Roth, S. V. Manipulating the Assembly of Spray-Deposited Nanocolloids: In Situ Study and Monolayer Film Preparation. *Langmuir* **2016**, *32*, 4251−4258.
(33) Kim, S.; Hyun, K.; Struth, B.; Ahn, K. H.; Clasen, C. Structural Development of Nanoparticle Dispersion during Drying in Polymer Nanocomposite Films. *Macromolecules* **2016**, *49*, 9068−9079.
(34) Khapli, S.; Rianasari, I.; Blanton, T.; Weston, J.; Gilardetti, R.; Neiva, R.; Tovar, N.; Coelho, P. G.; Jagannathan, R. Fabrication of Hierarchically Porous Materials and Nanowires through Coffee Ring Effect. *ACS Appl. Mater. Interfaces* **2014**, *6*, 20643−20653.
(35) Roth, S. V.; et al. In Situ Observation of Cluster Formation During Nanoparticle Solution Casting on a Colloidal Film. *J. Phys.: Condens. Matter* **2011**, *23*, 254208.
(36) Buffet, A.; Rothkirch, A.; Döhrmann, R.; Körstgens, V.; Abul Kashem, M. M.; Perlich, J.; Herzog, G.; Schwartzkopf, M.; Gehrke, R.; Müller-Buschbaum, P.; Roth, S. V. P03, The Microfocus and Nanofocus X-ray Scattering (MiNaXS) Beamline of the PETRA III Storage Ring: The Microfocus Endstation. *J. Synchrotron Radiat.* **2012**, *19*, 647−653.
(37) Benecke, G.; Wagermaier, W.; Li, C.; Schwartzkopf, M.; Flucke, G.; Hoerth, R.; Zizak, I.; Burghammer, M.; Metwalli, E.; Müller-Buschbaum, P.; Trebbin, M.; Förster, S.; Paris, O.; Roth, S. V.; Fratzl, P. A Customizable Software for Fast Reduction and Analysis of Large X-ray Scattering Data Sets: Applications of the New DPDAK Package to Small-angle X-ray Scattering and Grazing-Incidence Small-angle X-ray Scattering. *J. Appl. Crystallogr.* **2014**, *47*, 1797−1803.
(38) Schaffer, C. J.; Palumbiny, C. M.; Niedermeier, M. A.; Jendrzejewski, C.; Santoro, G.; Roth, S. V.; Müller-Buschbaum, P. A Direct Evidence of Morphological Degradation on a Nanometer Scale in Polymer Solar Cells. *Adv. Mater.* **2013**, *25*, 6760−6764.
(39) Wang, W.; Song, L.; Magerl, D.; Moseguí González, D.; Körstgens, V.; Philipp, M.; Moulin, J.-F.; Müller-Buschbaum, P. Influence of Solvent Additive 1,8-Octanedithiol on P3HT:PCBM Solar Cells. *Adv. Funct. Mater.* **2018**, *28*, 1800209.
(40) Feoktystov, A. V.; Frielinghaus, H.; Di, Z.; Jaksch, S.; Pipich, V.; Appavou, M.-S.; Babcock, E.; Hanslik, R.; Engels, R.; Kemmerling, G.; Kleines, H.; Ioffe, A.; Richter, D.; Brückel, T. KWS-1 High-resolution Small-angle Neutron Scattering Instrument at JCNS: Current State. *J. Appl. Crystallogr.* **2015**, *48*, 61−70.
(41) Müller-Buschbaum, P. Grazing Incidence Small-angle Neutron Scattering: Challenges and Possibilities. *Polym. J.* **2013**, *45*, 34−42.
(42) Owens, D. K.; Wendt, R. C. Estimation of the Surface Free Energy of Polymers. *J. Appl. Polym. Sci.* **1969**, *13*, 1741−1747.
(43) Ahola, S.; Salmi, J.; Johansson, L.-S.; Laine, J.; Österberg, M. Model Films from Native Cellulose Nanofibrils. Preparation, Swelling, and Surface Interactions. *Biomacromolecules* **2008**, *9*, 1273−1282.
(44) Qi, Z.-D.; Saito, T.; Fan, Y.; Isogai, A. Multifunctional Coating Films by Layer-by-Layer Deposition of Cellulose and Chitin Nanofibrils. *Biomacromolecules* **2012**, *13*, 553−558.
(45) Pääkkö, M.; Ankerfors, M.; Kosonen, H.; Nykänen, A.; Ahola, S.; Österberg, M.; Ruokolainen, J.; Laine, J.; Larsson, P. T.; Ikkala, O.; Lindström, T. Enzymatic Hydrolysis Combined with Mechanical Shearing and High-Pressure Homogenization for Nanoscale Cellulose Fibrils and Strong Gels. *Biomacromolecules* **2007**, *8*, 1934−1941.
(46) Benselfelt, T.; Pettersson, T.; Wågberg, L. Influence of Surface Charge Density and Morphology on the Formation of Polyelectrolyte Multilayers on Smooth Charged Cellulose Surfaces. *Langmuir* **2017**, *33*, 968−979.
(47) Félix, O.; Zheng, Z.; Cousin, F.; Decher, G. Are Sprayed LbL-films Stratified? A First Assessment of the Nanostructure of Spray-assembled Multilayers by Neutron Reflectometry. *C. R. Chim.* **2009**, *12*, 225−234.
(48) Nordenström, M.; Fall, A.; Nyström, G.; Wågberg, L. Formation of Colloidal Nanocellulose Glasses and Gels. *Langmuir* **2017**, *33*, 9772−9780.
(49) Yoneda, Y. Anomalous Surface Reflection of X-Rays. *Phys. Rev.* **1963**, *131*, 2010−2013.
(50) Sjöstedt, A.; Wohlert, J.; Larsson, P. T.; Wågberg, L. Structural Changes During Swelling of Highly Charged Cellulose Fibres. *Cellulose* **2015**, *22*, 2943−2953.
(51) Ehmann, H. M. A.; Werzer, O.; Pachmajer, S.; Mohan, T.; Amenitsch, H.; Resel, R.; Kornherr, A.; Stana-Kleinschek, K.; Kontturi, E.; Spirk, S. Surface-Sensitive Approach to Interpreting Supramolecular Rearrangements in Cellulose by Synchrotron Grazing Incidence Small-Angle X-ray Scattering. *ACS Macro Lett.* **2015**, *4*, 713−716.
(52) Kontturi, E.; Suchy, M.; Penttilä, P.; Jean, B.; Pirkkalainen, K.; Torkkeli, M.; Serimaa, R. Amorphous Characteristics of an Ultrathin Cellulose Film. *Biomacromolecules* **2011**, *12*, 770−777.
(53) Tammelin, T.; Abburi, R.; Gestranius, M.; Laine, C.; Setälä, H.; Österberg, M. Correlation Between Cellulose Thin Film Supramolecular Structures and Interactions with Water. *Soft Matter* **2015**, *11*, 4273−4282.
(54) Johansson, L.-S.; Tammelin, T.; Campbell, J. M.; Setälä, H.; Österberg, M. Experimental Evidence on Medium Driven Cellulose Surface Adaptation Demonstrated Using Nanofibrillated Cellulose. *Soft Matter* **2011**, *7*, 10917.
(55) Niinivaara, E.; Faustini, M.; Tammelin, T.; Kontturi, E. Water Vapor Uptake of Ultrathin Films of Biologically Derived Nanocrystals: Quantitative Assessment with Quartz Crystal Microbalance and Spectroscopic Ellipsometry. *Langmuir* **2015**, *31*, 12170−12176.
(56) Blell, R.; Lin, X.; Lindström, T.; Ankerfors, M.; Pauly, M.; Felix, O.; Decher, G. Generating in-Plane Orientational Order in Multilayer Films Prepared by Spray-Assisted Layer-by-Layer Assembly. *ACS Nano* **2017**, *11*, 84−94.
(57) Young, T. An Essay on the Cohesion of Fluids. *Philos. Trans. R. Soc. London* **1805**, *95*, 65−87.
(58) Van Oss, C. J.; Good, R. J.; Chaudhury, M. K. The Role of Van der Waals Forces and Hydrogen Bonds in Anhydrophobic Interactions Between Biopolymers and Low Energy Surfaces. *J. Colloid Interface Sci.* **1986**, *111*, 378−390.
(59) Zhang, S.; Ye, L.; Zhang, H.; Hou, J. Green-solvent-processable Organic Solar Cells. *Mater. Today* **2016**, *19*, 533−543.
(60) Zhang, S. S. A Review on the Separators of Liquid Electrolyte Li-ion Batteries. *J. Power Sources* **2007**, *164*, 351−364.
(61) Wenzel, R. N. Resistance Of Solid Surfaces To Wetting By Water. *Ind. Eng. Chem. Res.* **1936**, *28*, 988−994.

DOI: 10.1021/acs.macromol.9b00531
Macromolecules 2019, 52, 4721−4728